MICROSTRUCTURE AND MECHANICAL PROPERTIES OF LASER CLADDING REPAIR OF AISI 4340 STEEL

Shi Da Sun*, Qianchu Liu, ****, Milan Brandt*, ****, Madabhushi Janardhana***, and Graham Clark***

RMIT University, **Defence Science Technology Organisation (DSTO), *** Directorate General Technical Airworthiness (DGTA), * Defence Material Technology Centre (DMTC)**

stephen.sun@sudent.rmit.edu.au; qianchu.liu@dsto.defence.gov.au

Keywords: *Laser cladding, AISI 4340 steel, microstructure*

Abstract

Laser cladding (LC) was used to investigate the repair of high strength steel in aircraft applications, such as landing gears. This paper reports on the microstructure and microhardness properties of the deposited AISI 4340 clad layer on AISI 4340 steel substrate. Microhardness results showed the clad layer was 30-40% harder than the base material. Stress relieving the clad allowed the clad and HAZ areas to soften 10% below the base material. High dilution provided a favorable result on the hardness at the interface.

1 Introduction

High strength steels such as AISI 4340 are used widely in aircraft, particularly in critical applications such as landing gear. However they are known to be vulnerable to corrosion, impact and they are fracture-sensitive [1]. In aerospace applications such as critical carry-through structures, discovering even a small crack will lead to the reduction in airworthiness, and it is therefore vital to repair even small damage features, or replace the component. A repair by grinding out the damage may exceed dimensional limits, and where this happens, and in order for the aircraft to remain in service, it is usual to replace the damaged component. As the cost of replacing the component can be high, potential methods for repair by rebuilding the damaged area and restoring strength are of interest.

A potential repair technology is laser cladding. The concept is to melt a metal powder, with appropriate mechanical properties, using a laser beam, to form a track of solid metal fused with the substrate material to form a metallurgical bond [2]. There has been great interest in using laser cladding as a repair method for aerospace applications [3, 4].

Several researchers have reported on laser cladding of high strength steel. Bhattacharya et al. [5] has reported on the microstructural features of laser clad AISI 4340 steel powder on mild steel substrate powder on substrate. Other research on AISI 4340 steel has involved in laser melting application [6, 7]. Fastow et al. [6] analysed the microstructural and microhardness evolution of AISI 4340 steel when laser melted using a 1.2kW CO_2 laser. McDaniels et al. [7] showed that the HAZ of a laser melted AISI 4340 steel did not have an adverse effect on the fatigue properties.

However, very little research has been published on the repair of laser cladding of aero-grade high strength steel. This paper focuses on the mechanical properties of laser cladding of AISI 4340 steel powder on AISI 4340 aero-grade steel substrate. Microstructural features and microhardness properties are analysed. The aim is to; (i) Identify microhardness and microstructure evolution of high strength steel. (ii) Effect of the laser processing parameters on the microhardness and microstructure.

2 Experimental details

2.1 Material preparation

AISI 4340 steel plates of dimension 180 mm x 100 mm x 6 mm (composition shown in Table. 1) were supplied in annealed condition The plates were then heat-treated, in accordance with ASM handbook [8], by quench hardening and tempering to achieve a representative in-service UTS level of 1400MPa.

Table. 1. Chemical compositions (in wt. %) of the AISI 4340 base material as provided by supplier.

C	Mn	Ni	Cr	Si	Mo	V	Fe
0.41	0.7	1.74	0.77	0.24	0.25	0.046	Bal

AISI 4340 powder was supplied by Sandvik Osprey Ltd. in the form of gas atomized spherical particles (-106+45µm).

2.2 Laser cladding

A 4kW IPG Photonics fibre laser with a co-axial powder delivery head was used to deposit each clad. A mixture of helium and argon was used as both the carrier and shielding gas. The shielding gas flow was 15L/min. A 16.0mm standoff height (distance between the tip of the cladding head and the melt pool) was used. The cladding head was tilted 5° relative to the melt pool in order to minimize any back reflections from the melt pool damaging the laser.

Each plate was cladded in the direction of rolling. A 5.0mm bead width and a 2.5mm overlap were used to clad. The approximate track length was 23mm.

2.3 Metallurgical procedure

Samples were cross-sectioned, mounted, polished to 1.0µm finish and etched with a 4% Nital solution, in accordance with standard metallographic procedures [9]. Microscopic examination was conducted using a Leica MEF3 optical microscope.

Microhardness measurements were performed using a LECO LM700AT micro-hardness tester. An applied load of 300gf was held for 15 seconds, in accordance with standard ASTM procedure [10].

2.4 Experiment design

A total of three design conditions were used for the analysis of microstructure and micro-hardness: (i) Baseline (ii) clad layer with 2 different laser processing parameters (iii) post heat treatment (PHT).

The laser processing parameters used for repair are those that produce defect free clad layer. Any clad defects such as porosity and micro-cracking could act as damaging stress concentrators and degrade the mechanical properties of the material. Two laser processing parameters are tested (Table. 2).

Table. 2. Laser processing parameters used for this research.

No.	Powder flow rate (g/min)	Laser speed (mm/min)	Laser power (kW)	Laser beam diameter (mm)
1	25	1400	4	5
2	20	800	4	5

The laser processing parameters were determined from initial trials of AISI 4340 steel cladding [11]. Since the aim was to determine the optimum clad, no grind-out area was employed in the initial trials. In Fig. 1a, the clad/HAZ fusion line is where the red region contacts the green region and dilution/HAZ fusion line is where the yellow region contacts the green region. The inconsistent dilution is due to the Gaussian laser intensity distribution, causing a higher temperature in the center of the clad track, where most of the energy is supplied [12]. Parameter 1 is a low dilution clad (Fig. 1b) and parameter 2 is a high dilution clad (Fig. 1c). Dilution (D) is the percentage of area that has melted into the base material (Eq. 1).

$$D = \frac{A_D}{A_C + C_D} \cdot 100 \qquad (1)$$

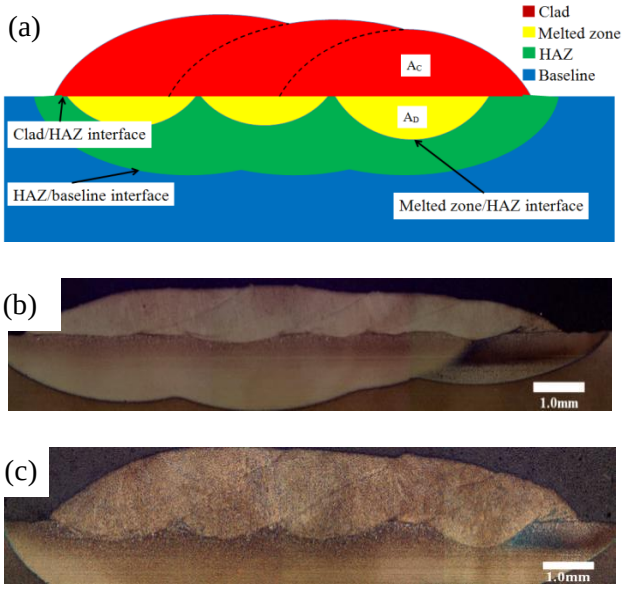

Fig. 1. (a) Schematic of a cross-sectioned multi-track clad (without grind-out) showing the 4 composite layers in a laser cladding process. (b) Clad 1. (c) Clad 2.

It is often reported when laser cladding to keep dilution to a minimum to minimize the mixing between the clad layer and the substrate in order to maintain the properties of the baseline material [13]. However, high dilution allows stronger bonding between the clad and base material and in some case may have beneficial properties [14]. It is known that in laser cladding the weakest point is the clad/HAZ interface due to inconsistent dilution/fusion [7, 15]. This research examines the effect of dilution on the hardness and static strength properties.

Residual stress and hardness variation occur in laser cladding due to high thermal gradients inherent in the process [16]. Residual stresses in clad material could affect the component's resistance to corrosion and fatigue cracks due to high thermal stress concentration. Post heat treating reduces the generated stresses at the clad/substrate interface and improves its mechanical properties. Post heat treatment was performed in accordance with ASM handbook standard [17] The process involved heating the clad plates to 560°C, and soaking for 3 hours followed by slow cooling to 250°C over 5 hours, and finally air cooling.

3 Results & discussion

3.1 Microstructure properties

3.1.1 Microstructure of the clad

For low alloy steel, the solidification structure consists of austenite dendrites and depending on the cooling rate, various other phases. The formation of a clad is dependent in part on the heating time which is influenced by the laser scan speed and is usually between 0.1-2 seconds [18]. The cooling rates of laser cladding are rapid usually between 10^3-10^6 k/s [19, 20]. For such high cooling rates with AISI 4340 steel material it is expected that the martensite structure to dominate the clad. Bhattacharya et al. [5] identified ferrite, martensite, and cementite phases in the microstructure of an AISI 4340 steel clad. Fastow et al. [6] showed that decreasing dilution generally results in a finer microstructure.

Fig. 2 shows that the clad layer consists of austenitic dendrites (white lines) where the growth is in the direction of solidification. Two distinct dendrite structures appeared in one single track clad; (i) cellular (Fig. 2a) and (ii) columnar (Fig. 2b). Dendritic formation is dependent on the heating and cooling rates. Heating and cooling rates are much more rapid near the surface [21] and temperature gradients generally exist across the solidifying structure resulting in the formation of different dendrites. A fine martensitic phase appeared within the dendrites due to rapid cooling rates. The black needles are constituents of bainite.

The dilution zone is a mixture of melted base material and clad powder. Since the powder and base material have similar chemical composition, the dilution zone has similar microstructural features to the clad zone.

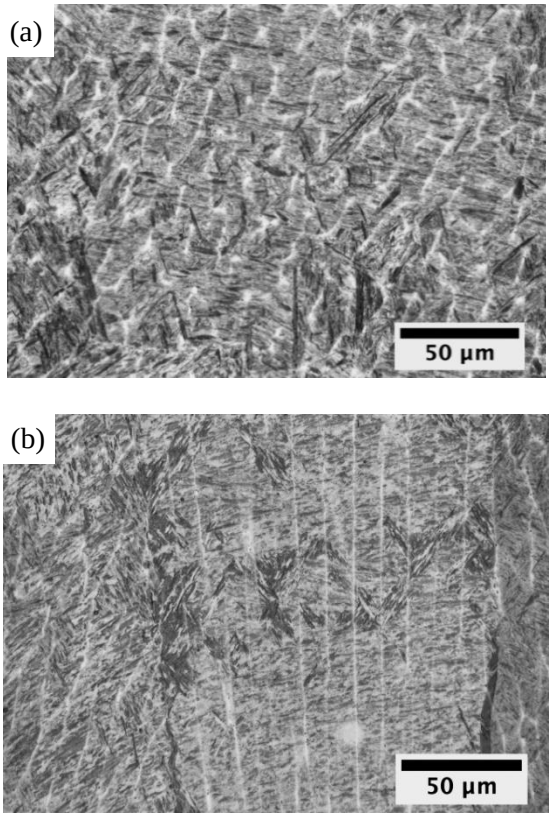

Fig. 2. Clad 2 parameters-20g/min, 800mm/min, 4kW (a) clad zone showing dendritic cellular structure (white lines) martensite (light grey areas between the dendrites) and bainite (dark needles) (b) clad zone with dendritic columnar structure.

3.1.2 Microstructure of the Heat Affected Zone

The HAZ is a complex heat treated area subjected to rapid heating with a short interaction time, followed by air cooling at room temperature during each pass. The heat treatment is similar to rapid quenching in air but using a range of heating temperatures. The HAZ starts from the clad/HAZ interface (Fig. 1a) where the peak temperature is just below the melting temperature of 0.4wt%C steel which is 1500°C (A_M) [22]. The temperature decreases proportionally to the HAZ depth, where according to the iron-carbon phase transformation diagram (Fig. 3), for a 0.4wt%C steel, the material will undergo γ and α phase transformation (γ at 800°C-1500°C, γ + α at 727°C-800°C) until the HAZ reaches the HAZ/baseline interface (Fig. 1a), where the cooling temperature reaches below the eutectoid temperature 727°C (A_1) which is the minimum temperature for γ transformation. Depending on the cooling rate, a variety of constituents may form such as martensite and bainite.

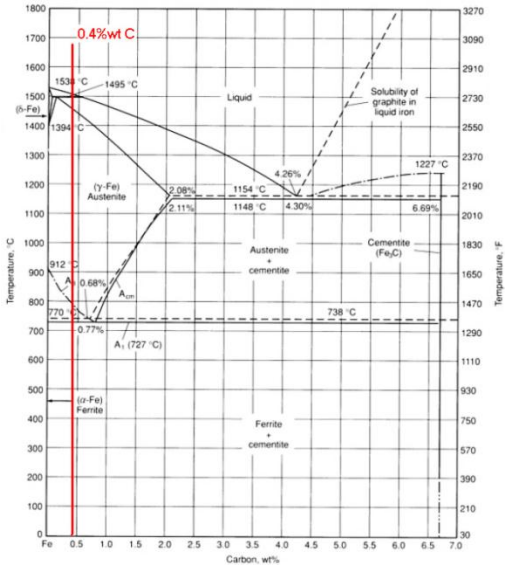

Fig. 3. Iron carbon transformation diagram. Red line indicates the phase transformations for AISI 4340 steel [23].

Directly below the clad/HAZ interface, where the peak temperature is just below A_M, the microstructure transformed to a coarser γ and upon cooling, transformed to an acicular ferrite (white needles) and lath martensitic/bainite structure (grey/dark regions), as shown in Fig. 4a. The martensite that formed is generally brittle due to the rapid cooling rate in air, and as a result, exhibits low ductility and toughness [8]. The coarsening of the γ grains near the clad/HAZ fusion line is due to high peak temperatures and causing high kinetic movement of atoms just adjacent to the clad/HAZ fusion line [24]. The coarsened HAZ caused significant grain growth, and as a result, the constituents of ferrite transformed into a more acicular appearance. The coarsening near the clad/HAZ interface is observed in welding [24] and other laser material processing where high heating temperature is applied [6]. Further away from the clad/HAZ interface, the grain size becomes finer due to decreased temperatures, and a traditional microstructure of a rapid quench heat treatment is observed (Fig. 4b).

The HAZ/baseline interface is distinctly identified (Fig. 4c), since transformation ceases when the temperature falls below A_1, where austenite transformation stops. The dark region is a microstructure of the baseline AISI 4340 steel prior to cladding. The white appearance in Fig. 4a is due to α constituent, where the heating temperature is just above A_1, consisting of γ + α transformation.

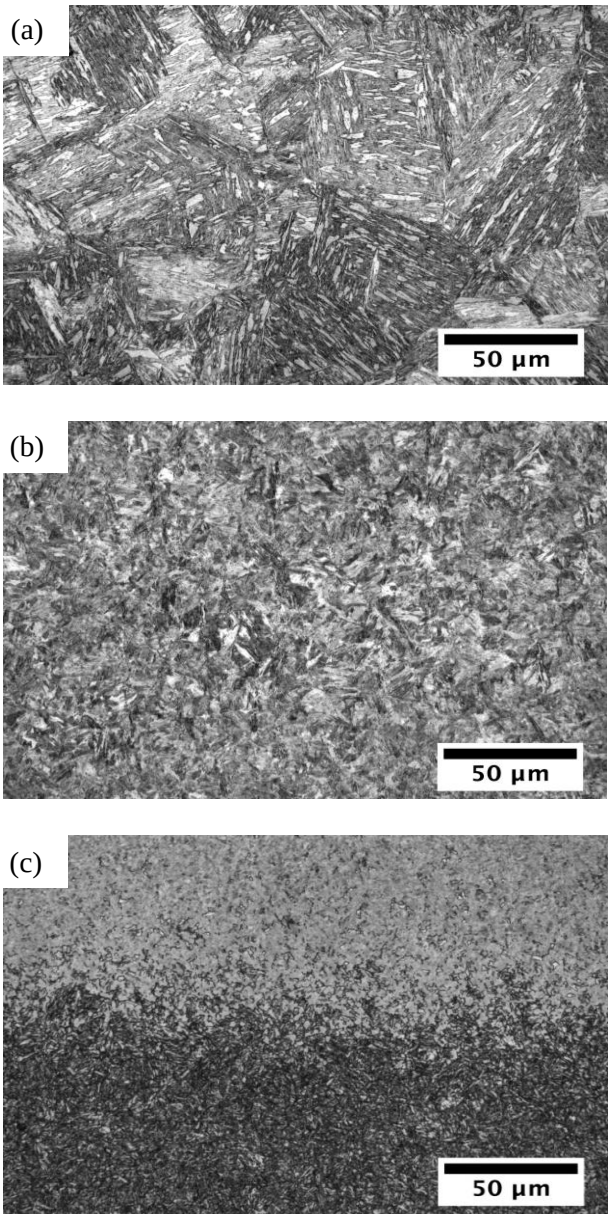

Fig. 4. Clad 2 parameters-20g/min, 800mm/min, 4kW. Microstructure evolution of the HAZ. (a) 0.2mm below the clad/HAZ interface. (b) 0.6mm below the clad/HAZ nterface. (c) HAZ/baseline interface.

3.1.3 Microstructure of Post Heat Treated (PHT) sample

The microstructure of the PHT clad and HAZ consisted mainly of α constituent, which is expected since the heating temperature of 560°C causes α transformation (Fig. 5). The acicular appearance of the ferrite is due to the longer heating time of the PHT procedure. The HAZ still maintained the coarsened γ grains near the clad/HAZ fusion line, as shown in Fig. 5b-c, which is expected since no γ transformation occurs in tempering.

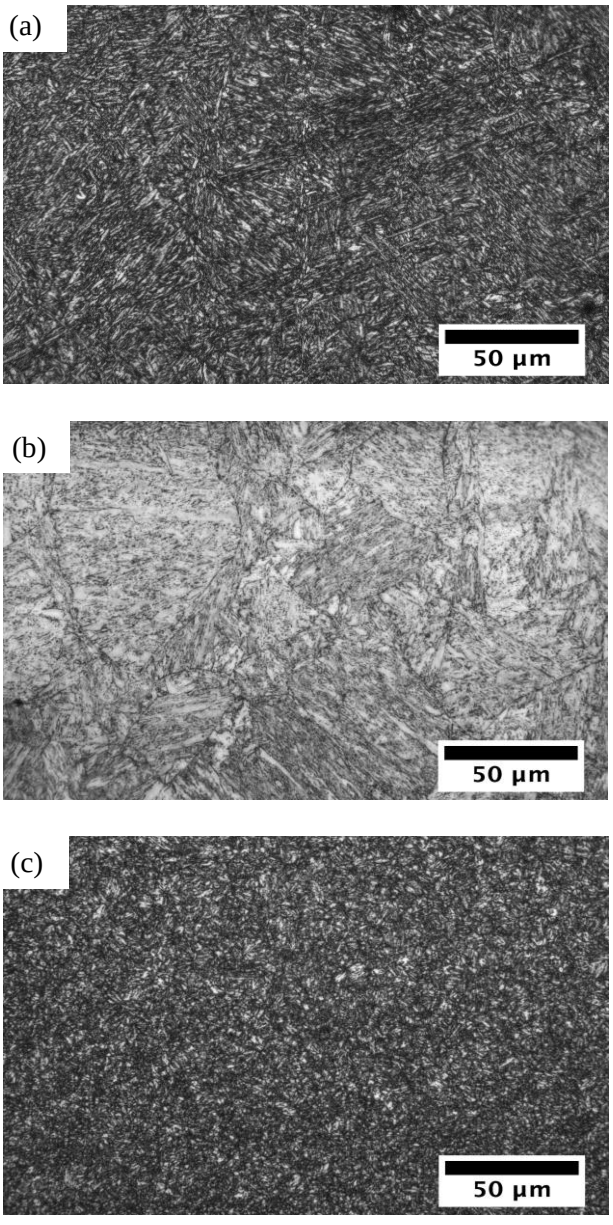

Fig. 5. Clad 2 parameters-20g/min, 800mm/min, 4kW. Microstructure of PHT of AISI 4340 steel (a) clad (b) 0.2mm below the clad/HAZ

interface (c) 0.6mm below the clad/HAZ interface.

3.2 Microhardness properties

3.2.1 General microhardness

Fig. 6 shows that the hardness of the clad was 30-40% higher than the base material. The high hardness in the clad was associated with martensite formed during rapid cooling of the melt pool (Fig. 2a). The average hardness of the dilution zone was similar to the clad.

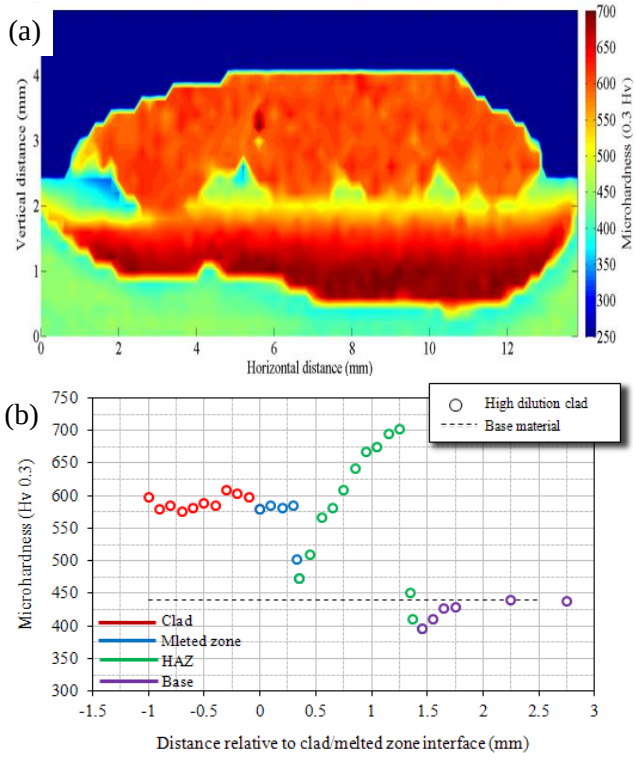

Fig. 6. (a) Microhardness contour plot of a multi-track clad area. Each indent was spaced out by 200µm. (b) Vertical microhardness profile, measured relative from the clad/melted zone interface (20g/min, 800mm/min, 4kW).

The hardness of the HAZ significantly increases almost linearly from the clad/HAZ interface to the HAZ/baseline interface, from 460Hv to 700Hv respectively, as shown in the green region in Fig. 6. The linear increase of the hardness in the HAZ is due to the heating temperature gradient in the HAZ causing a difference in grain growth. As discussed in section 3.1.2, a coarser microstructure is produced near the clad/HAZ interface due to high peak temperatures. The microstructure becomes finer away from the clad/HAZ nterface due to decreasing heating temperatures. A finer grain size is generally harder than a coarse grain size (Petch-Hall grain size effect [25, 26]). A similar microhardness trend in the HAZ was observed in laser melting of AISI 4340 steel [7].

The HAZ linearly increases to a maximum hardness of 700Hv, which is a similar hardness produced during a normal rapid quench hardening heat treatment process, where the heating temperature is between 815°C to 870°C [8]. Eventually the temperature reaches A_1 and hence no γ transformation occurs. As a result, at the end of the HAZ, a sharp drop in hardness occurs to near substrate conditions (380Hv). However, the hardness at the end of the HAZ is still 60Hv softer than the hardness of the substrate material. The softening is due to partial stress relieving/tempering which occurs just below the HAZ. The temperature just below the HAZ experiences similar heating temperatures for stress relieving of low alloy steel which is approximately between 595°C to 675°C [17] causing α transformation and softening the base material. The stress relieving effect fades after 0.5mm below the HAZ and the properties return to substrate condition.

3.2.2 The effect of dilution on microhardness

Fig. 7 showed that, for the low dilution (D=10%), the average clad hardness was approximately 650Hv. For a high dilution (D=30%), the average clad hardness was approximately 580Hv. D was calculated from Eq.1. The decrease of clad hardness with increasing dilution is due to the slower cooling rates at higher dilution. Dilution is a complex function of laser power, process speed and powder mass flow rate. Dilution increases with decreasing laser speed, increasing power, and decreasing powder flow rate [11]. Increased dilution means higher and concentrated melt temperatures due to longer laser interaction time, resulting in higher heating and slower cooling rates of the clad. The faster the laser speed is, the faster the cooling rate [27]. The

hardness of steel decreases with longer cooling rate due to the decrease in martensite.

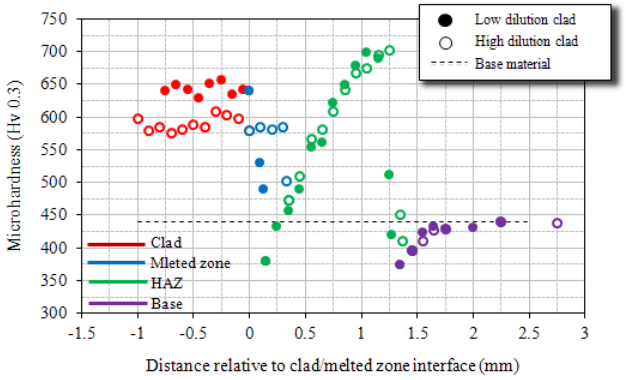

Fig. 7. Vertical microhardness profile, measured relative from the clad/melted zone interface showing the effect of dilution.

Other researches have also reported a variation of microhardness in a steel clad layer. In Sun et al. [28], the cladding with AISI 420 stainless steel substrate and satellite 6 clad showed the hardness of the clad is linearly dependent on the percentage of dilution. The hardness decreases linearly with increasing dilution which was due to an altered chemical composition of the clad layer from dilution. Similar results were found by Yellup [29]. The clad hardness of - stellite 6, Cenium Z20, and Eutrolloy – all decreased linearly when the dilution was greater than 10%. When the dilution was less that 10 %, the hardness of the clad was not altered.

Fig. 7 shows that at the melt zone/HAZ interface, a sharp drop in microhardness is experienced. For a low dilution, the hardness dropped to 380Hv. For a high dilution, the hardness dropped to 470Hv. The point measured was at the maximum melt depth of the sample. Since the cooling rate for a high dilution clad is slower than that of a low dilution clad, which means there was no time for grain growth to occur and as a result, a finer microstructure and a higher microhardness was obtained. High dilution had a favorable effect on the microhardness; (i) Clad is less brittle since the hardness was reduced as dilution increases. (ii) A smoother hardness transition occurs at the melted zone/HAZ interface. For low dilution, a high hardness differential is experienced where the hardness sharply drops from 650Hv to 380Hv. This differential of hardness acts as stress concentrator, which will degrade fatigue properties and also cause failure at the interface such as delamination.

3.2.3 The effect of PHT on microhardness

After PHT, both the clad and HAZ hardness decreased by 40% to 400Hv, which was approximately 40Hv below the hardness of the base material (Fig. 8). Since the coarsening of γ in the HAZ still exists, the HAZ maintained the linear increase of hardness, but only from 400Hv to a maximum of 460Hv at the end of the HAZ. A smooth hardness transition is experience at all the interfaces. PHT did not affect the hardness of the base material.

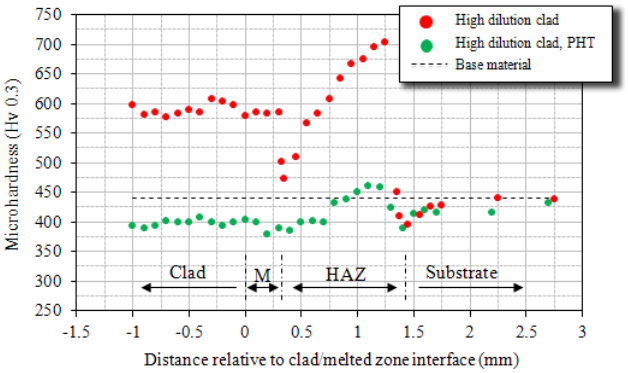

Fig. 8. Vertical microhardness profile, measured relative from the clad/melted zone interface showing the effect of PHT.

4 Conclusion

This study investigated the deposition of AISI 4340 steel powder on AISI 4340 high strength steel plate using laser cladding. Following conclusion can be made:

- The clad layer primarily consists of austenitic dendrites and fine martensitic and bainite structure, while the HAZ contained coarse austenite and an acicular martensitic/ bainitic structure.
- The hardness of the clad is 30-40% higher than the base material.

- Increasing dilution has a favourable effect on the hardness at the melted zone/HAZ interface.
- Increasing dilution from 10% to 30% decreases the average clad hardness from 650 to 580Hv.
- PHT decreased both the clad and HAZ hardness to 400Hv. A smooth hardness transition is experience between clad, HAZ and substrate.

5 Acknowledgement

The authors wish to acknowledge the financial and technical support of the Defence Science and Technology Organisation (DSTO) and Directorate General Technical Airworthiness (DGTA). In addition, the authors are indebted to the Industrial Research Institute Swinburne (IRIS), and Hardchrome Engineering for their assistance during the laser cladding trials.

References

[1] Hebsur M. Recent attempts of improving the mechanical properties of AISI 4340 steel by control of microstructure — A brief review, *Journal of Materials for Energy Systems*. Vol. 4, No. 1, pp 28-37, 1982.

[2] Sexton L, Lavin S, Byrne G and Kennedy A. Laser cladding of aerospace materials, *Journal of Materials Processing Technology*. Vol. 122, No. 1, pp 63-68, 2002.

[3] Liu Q, Janardhana M, Hinton B, Brandt M and Sharp K. Laser cladding as a potential repair technology for damaged aircraft components, *International Journal of Structural Integrity*. Vol. 2, No. 3, pp 314-331, 2011.

[4] Brandt M, Sun S, Alam N, Bendeich P and Bishop A. Laser cladding repair of turbine blades in power plants: from research to commercialisation, *International Heat Treatment and Surface Engineering*. Vol. 3, No. 3, pp 105-114, 2009.

[5] Bhattacharya S, Dinda G P, Dasgupta A K and Mazumder J. Microstructural evolution of AISI 4340 steel during Direct Metal Deposition process, *Materials Science and Engineering: A*. Vol. 528, No. 6, pp 2309-2318, 2011.

[6] Fastow M, Bamberger M, Nir N and Landkof M. Laser surface melting of AISI 4340 steel, *Materials Science and Technology*. Vol. 6, No. 9, pp 900-904, 1990.

[7] McDaniels R L, White S A, Liaw K, Chen L, McCay M H and Liaw P K. Effects of a laser surface processing induced heat-affected zone on the fatigue behavior of AISI 4340 steel, *Materials Science and Engineering: A*. Vol. 485, No. 1-2, pp 500-507, 2008.

[8] Bates C E, Wisti M and Hingwe M. Quenching & tempering of steel, *Heat Treating, ASM Metals Handbook*. Vol. 4, No. 1, pp 160-324, 1991.

[9] Bramfitt B L and Lawrence S J. Metallography and Microstructures of Carbon and Low-Alloy Steels, *Metallography and Microstructures, ASM Metals Handbook*. Vol. 9, No. 1, pp 608–626, 2004.

[10] ASTM Designation. E 384 Standard test method for microindentation hardness of materials. ASTM International. 1999.

[11] Sun S D, Brandt M, Liu Q, Janardhana M and Clark G. Process optimisation of laser assisted metal deposition of Aero-grade AISI 4340 steel, *(To be published)*, 2012.

[12] deLange D F, Hofman J T and Meijer J. Influence of intensity distribution on the meltpool and clad shape for laser cladding, *Proceedings of the Third International WLT-Conference on Lasers in Manufacturing*, Munich, Vol. 1, pp 1-5, 2005.

[13] Steen W M. *Laser material processing*. 3rd edition. Springer, 2003.

[14] Schneider M F. Laser cladding with powder; Effect of some machining parameters on clad properties, University of Twente, Ph.D Thesis, Enschede, The Netherlands, 1998.

[15] Pinkerton A, Wang W and Li L. Component Repair Using Laser Direct Metal Deposition, *Proceedings of the Institution of Mechanical Engineers, Part B: Journal of Engineering Manufacture*. Vol. 222, No.7, pp 827-836, 2008.

[16] Bendeich P, Alam N, Brandt M, Carr D, Short K, Blevins R, Curfs C, Kirstein O, Atkinson G, Holden T and Rogge R. Residual stress measurements in laser clad repaired low pressure turbine blades for the power industry, *Materials Science and Engineering: A*. Vol. 437, No. 1, pp 70-74, 2006.

[17] Canonico D A. Stress-Relief Heat Treating of Steel, *Heat Treating, ASM Metals Handbook*. Vol. 4, No. 1, pp 81-84, 1991.

[18] Ion J C. *Laser Processing of Engineering Materials: Principles, Procedure and Industial Application*. Elsevier Butterworth-Heinmann, 2005.

[19] Vilar R. Laser cladding, *Journal of Laser Applications*. Vol. 11, No. 2, pp 64-79, 1999.

[20] Ye X, Ma M, Liu W, Li L, Zhong M, Liu Y and Wu Q. Synthesis and Characterization of High-Entropy Alloy AlXFeCoNiCuCr by Laser Cladding, *Advances in Materials Science and Engineering*. Vol. 1, 2011.

[21] Aliya D and Lampman S. Physical metallurgy concepts in interpretation of microstructures, *Metallography and Microstructures in ASM Metal Handbook*. Vol. 9, No. 1, pp 44–70, 2004.

[22] Alloy Digest. ASM SA-14 AISI 4340 - Nickel Chromium Molybdenum Alloy Steel. ASM International. 1965.

[23] ASM Metals Handbook. Volume 1: Properties and selection irons steels and high performance alloys. ASM International. 1993.

[24] Vishnu P R. Solid-state transformation in weldment, *Welding, Brazing, and Solderi in ASM Metals Handbook*. Vol. 6, No. 1, pp 177-229, 2004.

[25] Hall E O. The deformation nd aging of mild steel, *Proceedings of the Physical Society B*. Vol. 63, 747-752, 1951.

[26] Petch N J. The cleavage strength of polycrystals, *Journal of Iron and Steel Institution*. Vol. 174, 25-28, 1953.

[27] Kim J D and Peng Y. Temperature field and cooling rate of laser cladding with wire feeding, *Journal of Mechanical Science and Technology*. Vol. 14, No. 8, pp 851-860, 2000.

[28] Sun S, Durandet Y and Brandt M. Parametric investigation of pulsed Nd: YAG laser cladding of stellite 6 on stainless steel, *Surface and Coatings Technology*. Vol. 194, No.2-3, pp 225-231, 2005.

[29] Yellup J M. Laser cladding using the powder blowing technique, *Surface and Coatings Technology*. Vol. 71, No. 2, pp 121-128, 1995.

Copyright Statement

This is the author pre-publication version. This paper does not include the changes arising from the revision, formatting and publishing process. The final paper that should be used for referencing is:

S. Ramasamy, M. Sangam, R. Sabatini, A. Gardi, "Flight Management System for Unmanned Reusable Space Vehicle Atmospheric and Re-entry Trajectory Optimisation", *Applied Mechanics and Materials*, vol. 629, pp. 304-309, Trans Tech Publications, 2014. DOI: 10.4028/www.scientific.net/AMM.629.304

Flight Management System for Unmanned Reusable Space Vehicle Atmospheric and Re-entry Trajectory Optimisation

Subramanian Ramasamy[1], Manoj Sangam[2], Roberto Sabatini[3,a*] and Alessandro Gardi[4]

[1,3,4] School of Aerospace, Mechanical and Manufacturing Engineering, RMIT University, Melbourne, VIC 3000, Australia

[2] Department of Aerospace Engineering, Cranfield University, Cranfield, MK43 0AL, United Kingdom

[a]roberto.sabatini@rmit.edu.au

Keywords: flight management system, unmanned reusable space vehicle, trajectory optimisation, re-entry trajectory planning

Abstract. The design and trajectory computation algorithms of an innovative Flight Management System (FMS) for Unmanned Reusable Space Vehicle (URSV) are presented. The proposed FMS features a number of functionalities in common with modern aircraft FMS that enable flight planning in non-segregated airspace, as well as specific features for optimal trajectory generation and space segment monitoring of the flight mission. The general avionics architecture of the URSV is presented and the specific FMS algorithms are developed to cope with the flight vehicle optimal trajectory planning and monitoring. Simulation case studies are performed in a realistic operational scenario resulting in the rapid generation of feasible trajectories, ensuring no violation of the defined mission and vehicle dynamics constraints. Additionally, an error budget analysis is performed on the longitudinal profile trajectories to evaluate the performance of the URSV.

Introduction

Unmanned platforms are being increasingly adopted for both atmospheric and space applications, despite the access to the civil airspace remains currently restricted to segregated areas. Similar to the manned aircraft versions, Flight Management System (FMS) for unmanned platforms is the core avionics component to introduce extensive automation algorithms for a number of Navigation, Guidance and Control (NGC) tasks. In this paper we propose an innovative FMS design, which incorporates both conventional aircraft FMS capabilities [1 – 3] and spacecraft re-entry trajectory generation algorithms, enabling non-segregated operations of an Unmanned Reusable Space Vehicles (URSV) in the civilian airspace. The Space Shuttle's entry guidance system [4] is used as a reference for re-entry trajectory planning. Guidance systems based on angle of attack (α) and bank angle (μ) modulations [5], on the quasi-equilibrium glide condition [6] and on the tracking of aerodynamic acceleration [7] have been developed. An improved methodology for re-entry trajectory planning based on creation of a drag acceleration profile as a function of energy has been developed [8] and is used as a baseline.

Avionic Systems Architecture

The avionic systems conceived for the URSV include an FMS, a Communications System (CS), a Flight Control System (FCS), a Mission Management System (MMS) for strategic/space orbital management, a Remote Piloting Management System (RPMS), which manages data exchanged via the CS to the remote Human Machine Interface and Interaction (HMI^2) station, an Obstacle Avoidance System (OAS) and a Rendezvous and Docking System (RVDS). The FCS translates the FMS/RPMS/OAS guidance or manual steering command inputs to actuators commands. Fig. 1 illustrates the functional architecture of the spacecraft avionic systems including the FMS subsystems listed in Table 1.

This is the author pre-publication version. This paper does not include the changes arising from the revision, formatting and publishing process. The final paper that should be used for referencing is:

S. Ramasamy, M. Sangam, R. Sabatini, A. Gardi, "Flight Management System for Unmanned Reusable Space Vehicle Atmospheric and Re-entry Trajectory Optimisation", *Applied Mechanics and Materials*, vol. 629, pp. 304-309, Trans Tech Publications, 2014. DOI: 10.4028/www.scientific.net/AMM.629.304

Table 1. FMS subsystems and associated functions.

FMS Subsystem	**Function**
Navigation Subsystem (NS)	Determines the state vector (position, attitude, linear and angular velocities) of the spacecraft incorporating a sensor suite, data fusion algorithms and processing logics.
Guidance Subsystem (GS)	Tracks the space vehicle's relative position from the validated trajectory and calculates vertical, turn and reinsertion manoeuvres wherever necessary.
Trajectory Planning and Optimisation Subsystem (TPOS)	Generates optimised atmospheric and re-entry trajectories based on the updated state (NS), dynamics (VDPS), ATM constraints (CS) and vehicle health (VHMS). A set of optimal trajectories is then dispatched to the RPMS and the TNVS for pilot and ATM evaluation and validation respectively.
Vehicle Dynamics and Performance Subsystem (VDPS)	Performs dynamics and performance calculations based on a multi-model architecture, which are primarily used by the trajectory planning/optimisation loop and for vehicle health assessment tasks.
Trajectory Negotiation and Validation Subsystem (TNVS)	Manages the negotiation and validation loops of 4-Dimensional Trajectories (4DT) through the CS with the ground-based ATM systems for safe operations in non-segregated airspace.
Surveillance Subsystem (SS)	Includes Automated Dependent Surveillance Broadcast (ADS-B) receiver and transmitter (In and Out) as well as legacy aeronautical surveillance devices.
Vehicle Data Management Subsystem (VDMS)	Manages data storage of all the spacecraft parameters and interacts with other subsystems for data retrieval and analysis.
Vehicle Health Management Subsystem (VHMS)	Manages the health conditions of the spacecraft by monitoring the data obtained from other components and dispatches reports to the RPMS for downlinking via the CS.
Vehicle Integrity Management System (VIMS)	Assesses and manages the integrity levels of Communication, Navigation and Surveillance (CNS) systems and generates caution and warning flags when the set threshold limits are exceeded.

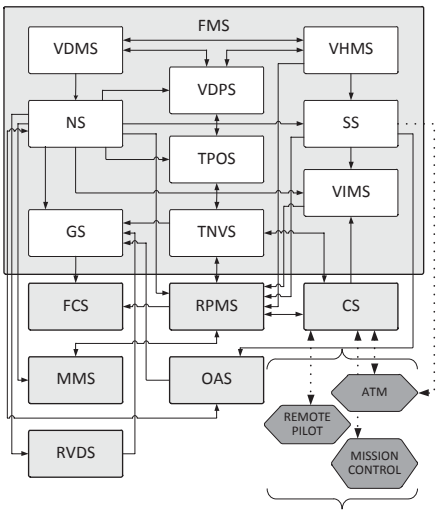

Fig. 1. Functional architecture of the URSV avionic systems.

This is the author pre-publication version. This paper does not include the changes arising from the revision, formatting and publishing process. The final paper that should be used for referencing is:

S. Ramasamy, M. Sangam, R. Sabatini, A. Gardi, "Flight Management System for Unmanned Reusable Space Vehicle Atmospheric and Re-entry Trajectory Optimisation", *Applied Mechanics and Materials*, vol. 629, pp. 304-309, Trans Tech Publications, 2014. DOI: 10.4028/www.scientific.net/AMM.629.304

The FMS performs optimal trajectory planning, negotiation and tracking tasks. The FMS interacts with the Air Traffic Management (ATM) system, remote pilot and mission control stations on the ground.

URSV Specifications

The URSV flight phases are designed as: flight in the lower atmosphere (up to 50 km), flight in the upper atmosphere until the Earth's environment (up to 250 km), flight beyond the Earth's environment (above 250 km till the orbit), flight in the designed orbital, initial descent re-entry and flight in the upper atmosphere, pseudo-equilibrium glide and TAEM phase. The URSV characteristics including the mission, and constraint data for re-entry and Terminal Area Energy Management (TAEM), are presented in Table 2.

Table 2. URSV characteristics and scenario parameters.

Parameter	Value
Vehicle Mass	16,177 kg
Reference surface	52.71 m^2
Nose radius	1 m
Re-entry Altitude	120 km
Re-entry Velocity	7764 m/s
TAEM Altitude	24.38 km
TAEM Velocity	743 m/s
Maximum Heat Flux	964 kW/m^2
Maximum g-load	2.5 g
Maximum Angle of Attack	45°
Re-entry mass	14,186 kg

Re-entry Trajectory Generation

The nominal re-entry phase of the URSV [9] begins at an altitude of around 120 km with a target speed of around Mach 25. The excessive energy is dissipated in order to attain the TAEM interface at the specified conditions. The re-entry is divided into two phases: initial descent and pseudo-equilibrium glide. Initial descent takes place from an altitude of 120 km to 80 km, where the atmospheric density is too low. During this phase, the vehicle experiences a controlled fall. Pseudo-equilibrium glide is a major portion of re-entry. The flight path angle is very small and all of the path constraints are taken into account in this phase. Since there is limited power to change α over a major portion of the hypersonic re-entry, modulation of μ is considered as the key control parameter. Banking manoeuvres provide an efficient way to dissipate excess energy and at the same time makes it possible to achieve the desired range. Based on the entry conditions, the actual state vector, path and dynamic constraints, a reference trajectory is generated by the TPOS consisting of altitude-velocity profile, drag acceleration profile. Reference altitude and velocity profiles are calculated by integrating the Equations of Motion (EoM). A reference α profile is identified. The re-entry energy corridor is then constructed based on the calculated upper and lower altitude/velocity limits. The necessary drag-energy profile is calculated and is used to determine the value of μ. Based on the μ profile, the trajectory is integrated up to the TAEM interface and the cross-range at TAEM interface is estimated. The objective of bank reversal logic is to minimise such cross-range error. By applying α and μ modulation and integrating the EoM, the complete trajectory is generated. A 3-degrees-of-freedom (3-DoF) point mass model is assumed as main real-time model implemented in the VDPS for URSV re-entry dynamics. The EoM incorporate two control variables $u = (\mu, \alpha)$. The six state variables are described as $x = [r, \theta, \varphi, V, \gamma, \psi]$. The 3-DoF point mass model EoM, governing the vehicle states, are given by:

$$\dot{r} = V \sin\gamma \tag{1}$$

This is the author pre-publication version. This paper does not include the changes arising from the revision, formatting and publishing process. The final paper that should be used for referencing is:

S. Ramasamy, M. Sangam, R. Sabatini, A. Gardi, "Flight Management System for Unmanned Reusable Space Vehicle Atmospheric and Re-entry Trajectory Optimisation", *Applied Mechanics and Materials*, vol. 629, pp. 304-309, Trans Tech Publications, 2014. DOI: 10.4028/www.scientific.net/AMM.629.304

$$\dot{\theta} = \frac{V \cos\gamma \sin\psi}{r \cos\varphi} \tag{2}$$

$$\dot{\varphi} = \frac{V \cos\gamma \cos\psi}{r} \tag{3}$$

$$\dot{V} = -D - (\sin\gamma \ / \ r^2) \tag{4}$$

$$\dot{\gamma} = \left(\frac{1}{V}\right)\left[L\cos\mu + \left(V^2 - \frac{1}{r}\right)\left(\frac{\cos\gamma}{r}\right)\right] \tag{5}$$

$$\dot{\psi} = \left(\frac{1}{V}\right)\left[\left(\frac{L\sin\mu}{\cos\gamma}\right) + \left(\frac{V^2}{r}\right)(\cos\gamma \ \sin\psi \tan\varphi)\right] \tag{6}$$

where 'r' is the radial distance from the centre of the Earth to the URSV in meters, 'θ' is the geodetic longitude in radians, 'φ' is the geodetic latitude in radians, 'V' is the velocity in m/s relative to the Earth surface, 'γ' is the flight path angle in radians and 'ψ' is the velocity azimuth angle in radians. The effect of wind and other atmospheric disturbances is assessed in the model validation. With the assumptions of no side-slip, non-rotating Earth and motion in vertical plane only (i.e., $\cos\mu = 1$), the EoM are simplified. The path constraints pertaining to heat flux, dynamic pressure and g-load form the upper boundary of the entry corridor. In general, we have:

$$\dot{Q} \leq \dot{Q}_{max} \tag{7}$$

$$|L\cos\alpha + D\sin\alpha| \leq n_{max} \tag{8}$$

where '$\dot{Q}_{max}$' is the max heat flux in W/m^2, 'n_{max}' is the max g-load factor, 'L' and 'D' are the lift and drag aerodynamic accelerations in m/s^2. The lower boundary of the corridor is given by the steady glide equilibrium and the higher boundary of the corridor is given by the lower of the following maximum drag accelerations [9] expressed as:

$$\left(g - \frac{V^2}{r}\right)\frac{C_D}{C_L} \leq D \leq \min\left\{\frac{\dot{Q}_{max}^2 C_D S}{2m\,C^2 V^4}; \frac{n_{max}\,g}{\frac{C_L}{C_D}\cos\alpha + \sin\alpha}; \frac{q_{max} C_D S}{m}\right\} \tag{9}$$

where 'q_{max}' is the maximum dynamic pressure in N/m^2, 'S' is the wing reference area in m^2, 'C_L' is the lift coefficient, 'C_D' is the drag coefficient, 'm' is the mass of the vehicle in kg and 'g' is the acceleration due to gravity in m/s^2. The constant 'C' is given by [9]:

$$C = \frac{(1.06584 \times 10^8)}{\sqrt{R_n \times \rho_0}} \frac{1}{(g \times r)^{1.5}} \tag{10}$$

where 'ρ_0' is the Atmospheric density at sea level in kg/m^3 and 'R_n' is the vehicle nose radius in m. A reference drag-acceleration profile is then generated such that the URSV lies within the entry corridor and takes into account a specified trajectory length. A 3-segment linear profile is adopted for the reference drag acceleration profile [9], where $D_1(E)$, $D_2(E)$ and $D_3(E)$ are the three drag segments. D_i and D_f are the initial and final values of drag acceleration respectively. E_i and E_f are the initial energy at re-entry and the final energy at TAEM interface respectively. D_c is the constant drag of the intermediate segment. E_1 and E_2 are the energies corresponding to the boundary values of the constant drag. The trajectory length, 'S' is given by:

$$S = \int_0^t V\,dt = -\int_{E_i}^{E_f} \frac{1}{D(E)}\,dE = \frac{E_1 - E_i}{D_i - D_c}\ln\frac{D_c}{D_i} + \frac{E_1 - E_2}{D_c} + \frac{E_f - E_2}{D_c - D_f}\ln\frac{D_f}{D_c} \tag{11}$$

By assuming an initial estimate of the trajectory length, the only unknown variable in the above equation is D_c, which is obtained by using the secant method [9]. Most of the re-entry algorithms assume a determined α profile. Though there is no specific method for determination of such profile, a general guideline is that α should be set close to its maximum value, α_{max} during the initial part of re-entry and it should be switched to $\alpha_{(L/D)_{max}}$ at a determined altitude before TAEM interface. The value of μ is derived from the constructed drag acceleration profile. The second derivative of drag acceleration with respect to energy is given by [8, 9]:

$$D'' = a + b\left(\frac{L}{D}\right)\cos\mu \tag{12}$$

This is the author pre-publication version. This paper does not include the changes arising from the revision, formatting and publishing process. The final paper that should be used for referencing is:

S. Ramasamy, M. Sangam, R. Sabatini, A. Gardi, "Flight Management System for Unmanned Reusable Space Vehicle Atmospheric and Re-entry Trajectory Optimisation", *Applied Mechanics and Materials*, vol. 629, pp. 304-309, Trans Tech Publications, 2014. DOI: 10.4028/www.scientific.net/AMM.629.304

where:

$$a = D\left(\frac{C_D''}{C_D} - \frac{C_D'^2}{C_D^2}\right) + D'\left(\frac{C_D'}{C_D} + \frac{2}{V^2}\right) - \frac{4D}{V^4} + \frac{1}{DV^2}\left(-\frac{1}{\rho}\frac{\partial\rho}{\partial r} + \frac{2g}{V^2}\right)\left(g - \frac{V^2}{r}\right) \quad (13)$$

$$b = -\frac{1}{V^2}\left(-\frac{1}{\rho}\frac{\partial\rho}{\partial r} + \frac{2g}{V^2}\right) \quad (14)$$

The heading of the vehicle relative to the desired heading at TAEM interface is continuously monitored and whenever the difference between the two exceeds a predefined threshold, the direction of μ is reversed. For evaluating the states with respect to tolerance values, error analysis was performed on the trajectories obtained in the longitudinal profile considering velocity, altitude and flight path angle deviations from the nominal value. The 2 σ error parameters used in the stochastic case are from [10, 11] and the 3-DoF vertical profile error parameters are expressed as:

$$\sigma_{\dot{V}} = \sqrt{\left(-\frac{1}{r^2}\cos\gamma\right)^2\sigma_\gamma{}^2 + \left(\frac{2\sin\gamma}{r^3}\right)^2\sigma_r{}^2 + \left(\frac{\rho V^2 S_{ref} C_{(D,\alpha)}}{2m}\right)^2\sigma_\alpha{}^2} \quad (15)$$

$$\sigma_{\dot{r}} = \sqrt{(\sin\gamma)^2\sigma_V{}^2 + (V\cos\gamma)^2\sigma_\gamma{}^2} \quad (16)$$

$$\sigma_{\dot{\gamma}} = \sqrt{\left(\frac{L\cos\mu}{V^2}\right)^2\sigma_V{}^2 + \left(-\frac{V\cos\gamma}{r^2} + \frac{\cos\gamma}{V.r^3}\right)^2\sigma_r{}^2 + \left(-\frac{V\sin\gamma}{r} + \frac{\sin\gamma}{V.r^2}\right)^2\sigma_\gamma{}^2 + \left(\frac{\rho V^2 S_{ref} C_{(L,\alpha)}}{2m}\right)^2\sigma_\mu{}^2} \quad (17)$$

where 'ρ' is the atmospheric density in kg/m^3 and 'S_{ref}' is the reference surface area of the URSV in m^2.

Simulation Results

After the reference altitude-velocity profile has been constructed imposing α to be constant at 45° and μ to zero, an entry corridor is identified in the drag-energy plane and the reference 3-segment drag acceleration profile is constructed for the vehicle under consideration as illustrated in Fig. 2. The upper boundary corresponds to the maximum heat flux and maximum g-loads. The lower boundary corresponds to the minimum lift. The updated α and μ profiles are obtained after the drag-energy profile is created. Angle of attack is set to a maximum of 45° during the initial part of re-entry to minimize heating and modulated near the TAEM interface to obtain the maximum lift-to-drag ratio. The total range covered in the re-entry phase is 9378 km. By using Monte Carlo sampling technique, the errors in the vertical profile are analysed for 100 samples and the mean and standard deviation [2 σ] values obtained for altitude, velocity and flight path angle are [21.29 m, 1.9937 m/s, 0.0000745 radian] and [29.82 m, 2.4357 m/s, 0.000616 radian] respectively. The results obtained from evaluating the errors demonstrate that the deviations are always well within the re-entry energy corridor.

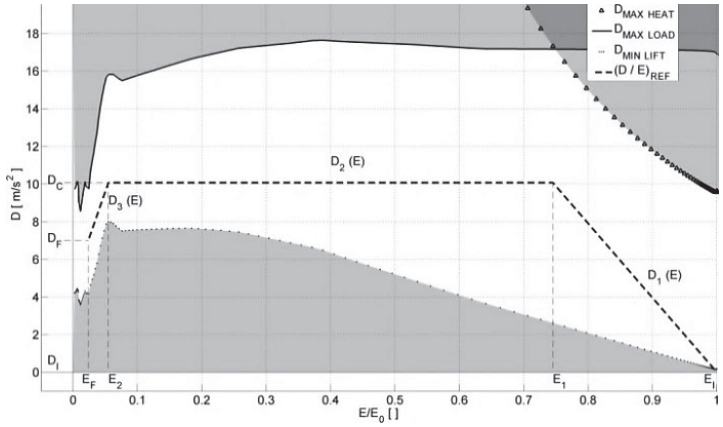

Fig. 2. Drag-energy profile construction.

This is the author pre-publication version. This paper does not include the changes arising from the revision, formatting and publishing process. The final paper that should be used for referencing is:

S. Ramasamy, M. Sangam, R. Sabatini, A. Gardi, "Flight Management System for Unmanned Reusable Space Vehicle Atmospheric and Re-entry Trajectory Optimisation", *Applied Mechanics and Materials*, vol. 629, pp. 304-309, Trans Tech Publications, 2014. DOI: 10.4028/www.scientific.net/AMM.629.304

Conclusions and Future Work

The architecture of a Flight Management System (FMS) of an Unmanned Reusable Space Vehicle (URSV) was presented, with a special focus on functionalities for trajectory planning for atmospheric re-entry. The different flight phases of the space vehicle were identified and hypersonic re-entry and Terminal Area Energy Management (TAEM) were addressed as the two major phases of the atmospheric re-entry. A novel on-board trajectory planning algorithm based on the drag-energy profile was developed for the hypersonic re-entry phase. Angle of attack (α) and bank angle (μ) modulation were used to shape the re-entry trajectory. Simulation case studies were performed for the re-entry phase and the results demonstrated the FMS suitability to generate efficient trajectory profiles that satisfy the given constraints. Future work is envisaged in including all other flight phases including orbital flight and to address the future 4D Trajectory Based Operations (4D-TBO) in an Environmentally Sustainable aviation (ESA) context [12].

References

[1] S. Liden, The Evolution of Flight Management Systems, AIAA/IEEE 13th Digital Avionics Systems Conference, Phoenix, AZ, USA. (1994) DOI: 10.1109/DASC.1994.369487

[2] J. Sorensen, The Flight Planning – Flight Management Connection, Proceedings of the American Control Conference, San Diego, CA, USA. (1984)

[3] A. Herndon, M. Cramer, K. Sprong and R. Mayer, Analysis of Advanced Flight Management Systems (FMS), Flight Management Computer (FMC) Field Observations Trials, Vertical Path, 26th Digital Avionics Systems Conference, Virginia, USA. (2007) DOI: 10.1109/DASC.2007.4391899

[4] J. Harpold and C. Graves, Shuttle Entry Guidance, Journal of the Astronautical Sciences, 37(3), pp. 239-268. (1979)

[5] J. Leavitt and K. Mease, Feasible Trajectory Generation for Atmospheric Entry Guidance, Journal of Guidance, Control and Dynamics, 30(2), pp. 473-481. (2007) DOI: 10.2514/1.23034

[6] Z. Shen and P. Lu, Onboard Generation of Three-Dimensional Constrained Entry Trajectories, Journal of Guidance, Control and Dynamics, 26(1), pp. 111-121. (2003) DOI: 10.2514/2.5021

[7] A. Saraf, J. Leavitt, D. Chen and K. Mease, Design and Evaluation of an Acceleration Guidance Algorithm for Entry, Journal of Spacecraft and Rockets, 41(6), pp. 986-996. (2004) DOI: 10.2514/1.11015

[8] K. Mease, D. Chen, P. Teufel and H. Schonenberger, Reduced-Order Entry Trajectory Planning for Acceleration Guidance, Journal of Guidance, Control and Dynamics, 25(2), pp. 257-266. (2002) DOI: 10.2514/2.4906

[9] M. Sangam, R. Sabatini, S. Ramasamy and A. Gardi, Advanced Flight Management System for an Unmanned Reusable Space Vehicle, International Journal of Unmanned Systems Engineering, 1(3), pp. 48-67. (2013) DOI: 10.14323/ijuseng.2013.11

[10] R. Sabatini, A. Kaharkar, C. Bartel and T. Shaid, Carrier-phase GNSS Attitude Determination and Control for Small UAV Applications, Journal of Aeronautics and Aerospace Engineering, 2(4). (2013) DOI: 10.4172/2168-9792.1000120

[11] R. Sabatini, M.A. Richardson, C. Bartel, A. Kaharkar, T. Shaid, L. Rodriguez and A. Gardi, A Low-cost Vision Based Navigation System for Small Size Unmanned Aerial Vehicle Applications, Journal of Aeronautics and Aerospace Engineering, 2(3). (2013) DOI: 10.4172/2168-9792.1000110

[12] S. Ramasamy, R. Sabatini, A. Gardi and Y. Liu, Novel Flight Management System for Real Time 4-Dimensional Trajectory Based Operations, AIAA Guidance, Navigation & Control Conference, Boston, Massachusetts, USA. (2013) DOI: 10.2514/6.2013-4763